ELSEVIER

Contents lists available at ScienceDirect

# Remote Sensing of Environment

journal homepage: www.elsevier.com/locate/rse



# Active layer freeze-thaw and water storage dynamics in permafrost environments inferred from InSAR



Jingyi Chen<sup>a,b,\*</sup>, Yue Wu<sup>a</sup>, Michael O'Connor<sup>b</sup>, M. Bayani Cardenas<sup>b</sup>, Kevin Schaefer<sup>c</sup>, Roger Michaelides<sup>d</sup>, George Kling<sup>e</sup>

- a Department of Aerospace Engineering and Engineering Mechanics, Cockrell School of Engineering, The University of Texas at Austin, Austin, TX, USA
- b Department of Geological Sciences, Jackson School of Geosciences, The University of Texas at Austin, Austin, TX, USA
- c National Snow and Ice Data Center, Cooperative Institute for Research in Environmental Sciences, University of Colorado at Boulder, Boulder, CO, USA
- <sup>d</sup> Department of Geophysics, Colorado School of Mines, Golden, CO 80401, USA
- <sup>e</sup> Department of Ecology and Evolutionary Biology, University of Michigan, Ann Arbor, MI, USA

#### ARTICLE INFO

#### Keywords: InSAR Permafrost Active layer Freeze-thaw cycle Soil water Vegetation cover

#### ABSTRACT

In cold regions where soils freeze and thaw annually, the ground surface deforms due to the density difference between groundwater and ground ice. Here we mapped thaw subsidence and frost heave signals over the Toolik Lake area on the North Slope of Alaska using 12 ALOS PALSAR Interferometric Synthetic Aperture Radar (InSAR) scenes (2006-2010). For the first time, we jointly analyzed InSAR observations with a large number of soil measurements collected within  $\sim 100$  km of the Toolik Field Station. We found that the InSAR-observed deformation patterns are mainly related to soil water content and the seasonal active layer freeze-thaw (FT) cycle. We did not observe any substantial long-term subsidence trend outside the 2007 Anaktuvuk River Fire scar. This suggests that the magnitude of the maximum annual thaw subsidence did not change much outside the fire zone during the study period. The joint analysis of InSAR and field observations allows us to show that the amplitude of the seasonal thaw subsidence is proportional to the total amount of ice that has melted into liquid water at any given time. We note that topography influences the spatial distribution of soil water content, and the availability of soil water influences the type of vegetation that can grow. As a result, we found that the average seasonal thaw subsidence increases along a geomorphic-ecohydrologic transect with heath vegetation on the drier ridgetops, tussock tundra on hillslopes, and sedge tundra at the wet lowland riparian zones. In addition, we detected a net uplift between late July and early September, mostly in the wetter riparian zone that experienced a larger seasonal thaw subsidence. Toolik Field Station in-situ records suggest that the air temperature fluctuated around or below freezing in early September during the ALOS PALSAR data acquisition times (at  $\sim 12$  am local time). In this scenario, ice can be formed at the top of the soil, which leads to frost heave in saturated soils. Our results highlight how InSAR can improve our understanding of active layer freeze-thaw and water storage dynamics in permafrost environments.

#### 1. Introduction

The delivery of water, carbon (C), and nutrients from the landscape to surface waters is a major component of global element cycles (Battin et al., 2009; Aufdenkampe et al., 2011). It fuels large fluxes of  $CO_2$  from inland waters to the atmosphere (Kling et al., 1991; Cole et al., 1994; Raymond et al., 2013), and delivers these elements to the world's oceans (Vonk and Gustafsson, 2013). Understanding the hydrological dynamics in northern latitudes is of particular concern because (i) C fluxes from arctic freshwaters may account for 40% of the net land

surface C exchange with the atmosphere (McGuire et al., 2009), (ii) climate change is thawing large areas of carbon-rich permafrost (Jorgenson et al., 2006), and (iii) thawing permafrost changes the hydrological connection of the land to rivers and lakes (Paytan et al., 2015; Neilson et al., 2018; O'Connor et al., 2019). There is widespread debate on how and when thawing soils in areas with permafrost, which store twice the amount of C found in the atmosphere (Ping et al., 2008), will contribute to the C cycle and amplify global climate change (Schuur et al., 2008; Macdougall et al., 2012). This debate is due in part to a limited understanding of specific hydrologic mechanisms

E-mail address: jingyi.ann.chen@utexas.edu (J. Chen).

<sup>\*</sup> Corresponding author at: Department of Aerospace Engineering and Engineering Mechanics, Cockrell School of Engineering, The University of Texas at Austin, Austin, TX, USA.

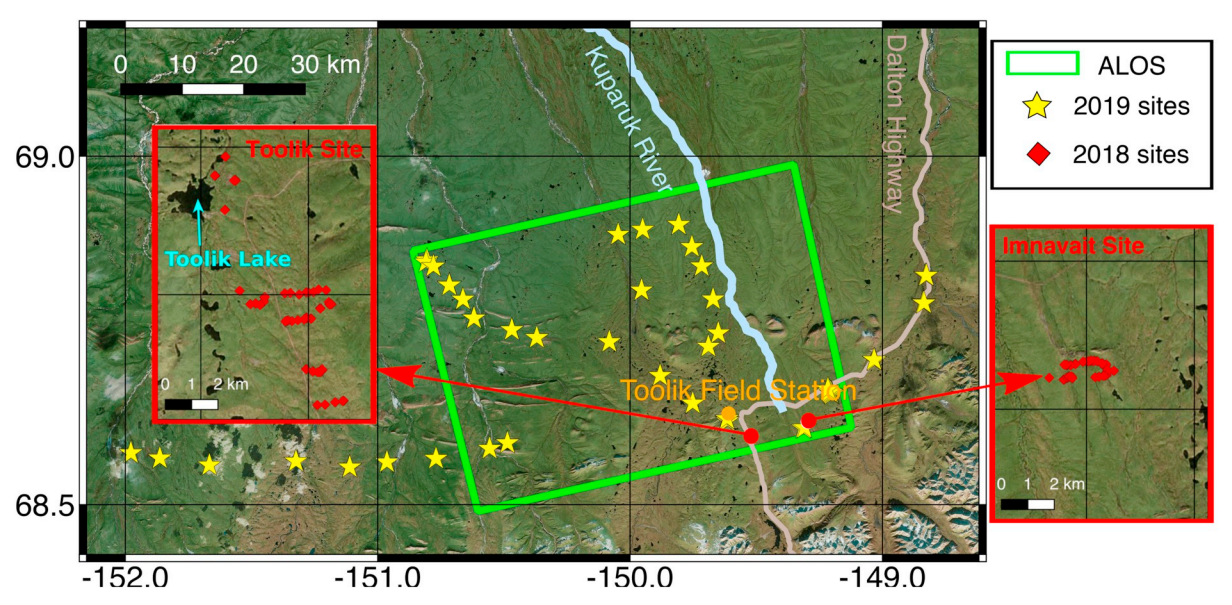


Fig. 1. A map of the study area in the upper Kuparuk River Basin near Toolik Lake on the North Slope of Alaska. The ALOS PALSAR data coverage (Path 255, Frame 1370) over the area of interest (~ 65 km × 45 km) is outlined in green. The 2018 sample sites (on foot) are marked as red diamonds, and the 2019 sample sites (by helicopter or on foot) are marked as yellow stars. Note that the Dalton Highway is the only accessible road in the area. (For interpretation of the references to colour in this figure legend, the reader is referred to the web version of this article.)

controlling water storage and transport from the land to surface waters (Alexander et al., 2007; McDonnell, 2003; Vidon et al., 2010; Fisher et al., 2018). The main mechanism for the net export of carbon from catchments in continuous permafrost to surface waters and then to the atmosphere and oceans is thought to be overland flow (McNamara et al., 1998). However, recent studies show that groundwater contributions can control dissolved organic carbon and nitrogen export from land to rivers and lakes (Neilson et al., 2018; Walvoord and Striegl, 2007). These groundwater contributions depend on the thickness of the "active layer", which controls groundwater storage and flow (O'Connor et al., 2019). Here the active layer is defined as any part of the ground layer above permafrost that freezes and thaws annually. Over the summer, thaw migrates downward at a rate controlled by heat inputs, insulation from vegetation, and soil characteristics (e.g., Sjoberg et al., 2016; Painter et al., 2016). At the end of the thawing season, the maximum thaw depth is defined as the active layer thickness (ALT).

The Arctic covers continent-sized areas that are mostly hard to access, and satellite remote-sensing has become an important tool for studying many processes in permafrost landscapes that are otherwise unobservable (Antonova et al., 2016; Chen et al., 2019; Bartsch et al., 2020). Interferometric Synthetic Aperture Radar (InSAR) techniques use two Synthetic Aperture Radar (SAR) satellite images over the same area to estimate surface deformation that occurs between two SAR acquisition times with 10s-100s of meters spatial resolution and millimeter-to-centimeter Line-Of-Sight (LOS) measurement accuracy (Rosen et al., 2000; Hanssen, 2001). Because groundwater takes up less volume than ground ice, the surface settles as the active layer thaws in summer, with the opposite occurring during freeze-up in fall (Liu et al., 2010; Short et al., 2011; Antonova et al., 2018; Strozzi et al., 2018; Rouyet et al., 2019). Furthermore, deepening of the maximum active layer or melting of excess ground ice can cause a long-term surface subsidence trend (Liu et al., 2014; Molan et al., 2018; Michaelides et al., 2019a; Liu et al., 2015; Iwahana et al., 2016). Based on this fact, Liu et al., 2012 and Schaefer et al., 2015 developed an InSAR-based ALT retrieval algorithm known as the Remotely-Sensed Active Layer Thickness (ReSALT) using a mixed organic and mineral fully-saturated soil model, and estimated ALT near Prudhoe Bay and Utqiagvik on the Alaskan North Slope with a height uncertainty of  $\sim 10$  cm. Following a similar approach, Daout et al., 2017 analyzed the temporal and spatial variations of the permafrost ALT on the Tibetan Plateau over a 60,000  $km^2$  region. They observed that the amplitude and timing of the seasonal subsidence associated with the annual active layer freeze-thaw (FT) cycle depended greatly on sediment type, with unconsolidated sediments having much higher subsidence than exposed bedrock. They also found a correlation between the amplitude of thaw subsidence and the topographic slope, but did not provide any in-situ validation of that correlation.

Previous studies have tended to associate larger seasonal thaw subsidence with larger active layer thickness. However, as reported in Daout et al., 2017, the amplitude and timing of the thaw subsidence and frost heave could depend on other factors such as sediment type and local topographic slope. The goal of this study is to determine the controls on InSAR deformation signals associated with the active layer freeze and thaw for different soils under different geomorphic and ecohydrologic settings based on in-situ observations. Because most of the Arctic is hard to access, the availability of data on soil characteristics is extremely limited (Ping et al., 2008). Our study is the first analysis that integrates spaceborne InSAR deformation data with a large number of soil measurements that contain relevant information on water holding capacity. This allows us to show that the amplitude of the maximum seasonal thaw subsidence is proportional to the equivalent water depth in the active layer near the end of thaw season. Because the amount of water in the active layer influences the type of vegetation that can grow, InSAR can thus help determine and monitor ecological characteristics of the permafrost terrain.

## 2. Site characteristics

The two major soil types in the Arctic are typically related to glacial age: most of the North American and European Arctic are characterized by young land surfaces exposed by recession of the last continental ice sheets or mountain glaciers (< 15,000 yr BP), whereas most of Siberia to far northwestern Canada represents older surfaces (> 100,000 yr BP) not glaciated during the late-Quaternary (Hamilton, 1975; Hamilton, 1986). The pattern of late-Quaternary glacial advances near Toolik Lake in the Upper Kuparuk River Basin on the North Slope of Alaska (Fig. 1) resulted in the juxtaposition of these two major soil ages and characteristics within a region exposed to similar climate. Currently, the more acidic tundra of older surfaces near Toolik (> 100,000 yr BP) has more extensive tussock tundra communities, shallower thaw layers,

and deeper organic soil accumulations compared to the younger, nonacidic tundra surfaces (< 15,000 yr BP) (Walker et al., 1989; Ping et al., 1998; Munroe and Bockheim, 2001). Furthermore, within the two main soil ages, several vegetation types grow on soils with distinct water holding capacities: (1) heath vegetation (e.g., evergreen prostrate shrubs) on the drier hilltops; (2) tussock tundra on the hillslopes; and (3) wet sedge tundra (sedge tundra) at the lowland valley bottoms. Since 1975, research in the area near Toolik Lake has studied the effects of both natural and anthropogenic environmental change on arctic landscapes. This past and current research provides a long-term database of many meteorological, ecological, and hydrological variables (Hobbie and Kling, 2014). In this study, we collected 220 in-situ soil samples at various sites within  $\sim 100$  km of the Toolik Field Station. We used the properties of these soil samples to calculate the expected seasonal thaw subsidence, which was compared with InSAR surface deformation estimates. The ALOS PALSAR spatial coverage and field sampling sites are marked in Fig. 1.

#### 3. Methods

#### 3.1. Surface deformation due to freezing and thawing of the active layer

The total volume of water S stored in the active layer can be expressed as (Liu et al., 2010):

$$S = Az_{\text{water}} = A \int_0^{ALT} s(z)\phi(z)dz$$
 (1)

where A is the unit area,  $z_{\rm water}$  is the equivalent water depth, ALT is the active layer thickness, and dz is the incremental thickness of the thawed soil column. Both the soil porosity  $\phi$  and the soil saturation ratio s (0–1) vary with soil depth z and together determine the vertical distribution of pore water within the soil column.

The maximum seasonal thaw subsidence  $\Delta d_{\rm season}$  is proportional to the equivalent water depth  $z_{\rm water}$  in the active layer as:

$$\Delta d_{\rm season} = \frac{\rho_w - \rho_i}{\rho_i} z_{\rm water} \approx 0.09 z_{\rm water}$$
 (2)

where  $\rho_w$  is the density of water, and  $\rho_i$  is the density of ice. For example, when a 10 cm liquid water column freezes, it expands by  $\sim$  9 mm. Following Eq. (1), a 10 cm soil column with 50% porosity and filled halfway with liquid water (equivalent to 50% saturation) contains the same amount of soil pore water as a 5 cm soil column with 50% porosity and filled to the top with liquid water (equivalent to 100% saturation). Thus we expect to observe 2 mm of thaw subsidence at the end of thaw season in both cases.

We next discuss key elements in the arctic water cycle that influence the distribution of water in soils (Fig. 2). The change in the active layer water storage  $\Delta S$  over a summer thaw season can be expressed as:

$$\Delta S = P - ET - Q + T \tag{3}$$

where P is precipitation (including snow melting), ET is evapotranspiration, Q is the runoff water leaving the soil and entering surface waters (rivers and lakes), and T is the amount of soil water increase due to thawing of permafrost. Here *P* includes both rain and snow, and the snow portion of P contributes to the active layer water storage at a delayed time during snow melting. The portion of *P* that directly goes to Q or ET does not lead to any change in the active layer water storage, and thus does not cause any thaw subsidence (the water is never turning into ice in the active layer). If the net water drainage is minimal  $(P - ET - Q \approx 0)$ , then only thaw deepening at the bottom of the active layer (into permafrost) that increases T can increase the active layer water storage and the maximum seasonal thaw subsidence. Alternatively, if the maximum thaw depth is stable or at the time of maximum thaw the active layer deepens into permafrost with very low or no ice content ( $T \sim 0$ ), then only a positive water flux (P - ET - Q > 0) can result in greater active later water storage and

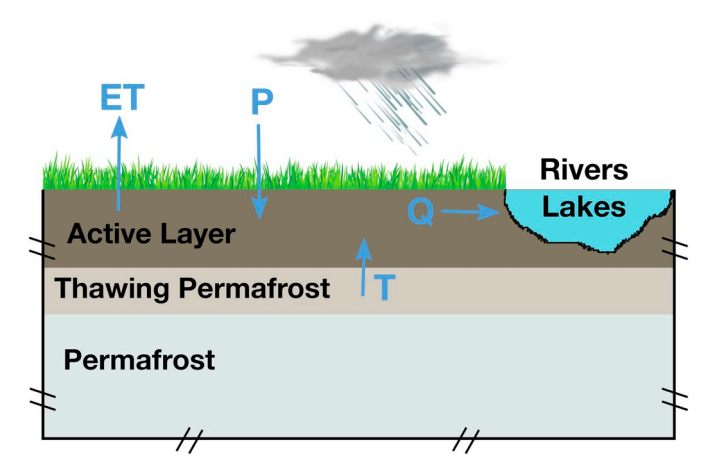


**Fig. 2.** The active layer water budget model. Here P is precipitation (including snow melting), ET is evapotranspiration, Q is the runoff water leaving the soil and entering surface waters (rivers and lakes), and T is the amount of soil water increase due to thawing of permafrost.

seasonal thaw subsidence.

#### 3.2. InSAR observations

#### 3.2.1. InSAR data processing strategy

Interferometric SAR (InSAR) computes the phase difference between two Synthetic Aperture Radar (SAR) images. The resulting interferogram can be used to infer a map of surface deformation between two SAR acquisition times (Rosen et al., 2000; Hanssen, 2001). We downloaded 30 L-band ALOS PALSAR scenes (Path 255 and Frame 1370) over the area of interest (Fig. 1) from the Alaska Satellite Facility. Note that there were no ALOS acquisitions available in February, May, and August during the study period 2006-2010. We excluded 3 scenes acquired on 22 July 2007, 24 July 2008, and 14 September 2010 because these scenes are heavily corrupted by distinctive ionospheric artifacts (Wegmüller et al., 2006; Fattahi et al., 2017). We also excluded all 15 winter scenes acquired between November to April because the observed phases in winter-winter interferograms are likely related to variations in snow accumulation and snow redistribution, which is not the focus of this study. The summer-winter interferograms are mostly decorrelated because the presence of snow cover can significantly change surface scattering properties. Information on Toolik ALOS PALSAR data properties is summarized in Table 1.

We processed the remaining 12 SAR scenes using a motion-compensation imaging radar processor developed by the Stanford radar interferometry group (Zebker et al., 2010) and generated all 66 multilooked interferograms (60 m resolution). This is equivalent to imposing a temporal baseline threshold of 1518 days (the time interval between the first and last ALOS PALSAR acquisitions), and a spatial baseline threshold of  $\sim$  13 km (the critical baseline for ALOS PALSAR FBS interferograms) (Sandwell et al., 2008). We removed the topographic phase using the Kuparuk River watershed Digital Elevation Model

**Table 1**Toolik ALOS PALSAR data properties.

Study period	2006–2010
Number of SAR scenes Available Acquisitions over the Toolik area Satellite revisit cycle Spatial resolution Wavelength Line-Of-Sight vector Viewing geometry	12 early June, late July, early September, late October 46 days 60 m (multi-looked) 24 cm (L-band) [0.61 0.13 - 0.78] at the mid-swath Ascending

(DEM; 25 m resolution) (Nolan, 2003). We unwrapped the interferograms using SNAPHU and a minimum-cost flow algorithm (Chen and Zebker, 2001). Some of the interferograms contain long-wavelength phase ramps across the image, possibly due to a residual orbit error, time tagging error, long-wavelength tropospheric and ionospheric noise, or tectonic motion. These ramps were removed using a planar phase model. In order to preserve as many interferograms as possible, we did not expose any threshold on temporal and spatial baselines. Instead, we inspected the quality of all interferograms, and excluded 8 interferograms with visible decorrelation artifacts and large phase unwrapping errors. For the remaining 58 interferograms, we masked out water bodies using the North Slope Science Initiative (NSSI) Landcover GIS Data. We did not impose any additional pixel masks based on InSAR phase coherence.

InSAR technique only measures a relative radar line-of-sight (LOS) deformation with respect to a selected pixel. We chose a reference point (68.83° N 150.23° W) where the minimum seasonal deformation was observed during the study period. Assuming no deformation at the reference point and little variation in the horizontal motion, we converted radar LOS deformation  $\Delta d_{\rm LOS}$  to vertical deformation  $\Delta d_{\rm vertical}$  based on:

$$\Delta d_{\rm LOS} = e_3 \Delta d_{\rm vertical} \tag{4}$$

where  $e_3$  is the third component of the radar LOS direction unit vector  $e = [e_1, e_2, e_3]$ . For the ALOS ascending imaging geometry over the Toolik area,  $e = [0.61 \ 0.13 \ -0.78]$  at the mid-swath. The look angle variation over the 40 by 60  $km^2$  study area is not substantial. We note that slope creep processes (e.g., Dini et al., 2019) may lead to nonnegligible horizontal motion in regions with large slope angles. Those pixels were identified and excluded in our analysis as discussed in Section 3.2.3.

#### 3.2.2. Long-term and seasonal freeze-thaw deformation solutions

The active layer is completely frozen between December and May each year. In early June, seasonal thaw starts to migrate downward. At a given time, the magnitude of the thaw subsidence is proportional to the total amount of ice that has melted into liquid water (Eq. (2)). When the active layer starts to freeze in the fall, frost heave can be observed. If the net water drainage is minimal  $(P - ET - Q \approx 0 \text{ in Eq. (3)})$ , the total amount of thaw subsidence equals the total amount of frost heave in a FT cycle. In the Toolik area, the maximum thaw occurs in mid-late August (Supplementary Materials S1). The thawing process and the associated thaw subsidence slows down around the time of maximum thaw. This is because the thermal diffusivity of ice is larger than that of the liquid water. As more water in the soil column becomes liquid, heat takes much longer to diffuse through the entire thawed soil column. In addition, the porosity and water holding capacity of soil typically decrease with depth (O'Connor et al., 2020). Therefore, late summer thaw in relatively dry soils typically does not cause substantial thaw sub-

We first consider a scenario where the active layer water storage and the magnitude of the maximum thaw subsidence increases over multiple FT cycles due to thawing of permafrost (Fig. 3a). If the radar satellite acquired two SAR scenes A and B in early June and late July in a single FT cycle, we can form an interferogram A-B that measures the seasonal thaw subsidence  $d_B-d_A$  that occurred between early June and early July of that year. If the radar satellite acquired another SAR scene C in late July of another FT cycle (another year), we can form two additional interferograms A-C and B–C. The observed deformation  $d_C-d_A$  of the interferogram A-C contains a seasonal component and the long-term trend across years. The observed deformation  $d_C-d_B$  of the interferogram B–C contains the long-term trend only.

In another scenario where the active layer water storage remains unchanged over multiple years (Fig. 3b), we can assume the InSAR deformation signals associated with the active layer freeze and thaw over multiple FT cycles are identical. In this case, interferograms that span the same month period contain the same thaw subsidence or frost

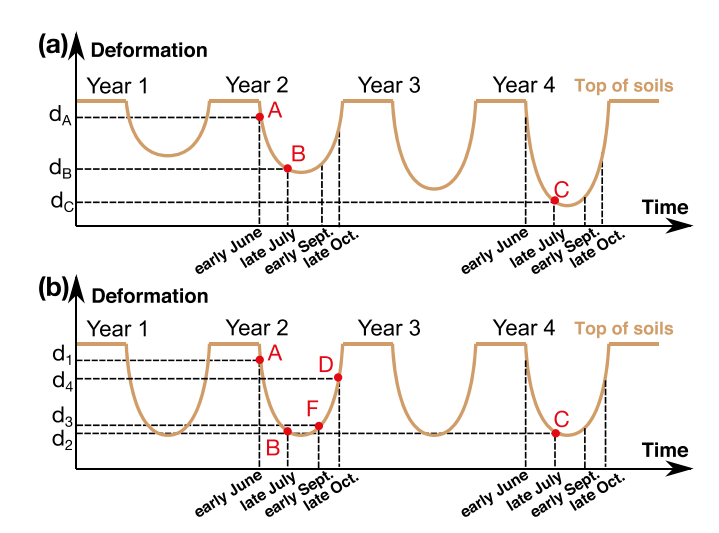


**Fig. 3.** Surface deformation (brown line, downward means subsidence) associated with the freeze-thaw (FT) processes of the active layer. Here we assume the net water drainage is minimal  $(P-ET-Q\approx 0)$ . Thus, the total amount of thaw subsidence equals the total amount of frost heave in a FT cycle. (a) A scenario where the active layer water storage increases over multiple years due to thawing of permafrost. A, B, and C correspond to three SAR acquisitions, and we can form an interferogram using any two SAR scenes to measure surface deformation that occurs between the two SAR acquisition times. (b) A scenario where the active layer water storage remains unchanged over multiple years. In this case, no long-term deformation trend is present. A, B, C, D, and F correspond to five SAR acquisitions. (For interpretation of the references to colour in this figure legend, the reader is referred to the web version of this article.)

heave signal. For example, both interferograms B-D and C-D measure the frost heave  $d_4-d_2$  that occurred between late July and early September, and both interferograms A-B and A-C measure the thaw subsidence  $d_2-d_1$  that occurred between early June and late July. Because both late July and early September are close to the time of maximum thaw subsidence,  $d_2 \approx d_3$ .

We first estimated the long-term subsidence trend v (cm/year) at a pixel of interest based on a stacking approach (Rouyet et al., 2019; Sandwell and Price, 1998; Peltzer et al., 2001; Lyons and Sandwell, 2003):

$$v = \frac{\sum (\Delta d_{\text{vertical},i})}{\sum (\Delta t_i)}$$
 (5)

where  $\Delta d_{\rm vertical,\ i}$  is the vertical deformation at this pixel as inferred from the  $i^{th}$  interferogram listed in Table 2 (left).  $\Delta t_i$  is the total number of years that the  $i^{th}$  interferogram spans. Note that all interferograms in Table 2 (left) span multiple FT cycles. These interferograms contain a minimal seasonal component, because they were generated using SAR scenes either around the same time of the year (e.g., the 2006/10/19–2007/10/22 pair) or around the time of maximum thaw (e.g., the

**Table 2**Interferograms used for estimating the average long-term and seasonal deformation.

Long-term stack	Seasonal Stack	
2006/10/19-2007/10/22 2006/10/19-2008/10/24 2006/10/19-2009/10/27 2007/09/06-2009/07/27 2007/09/06-2009/09/11	2006/06/03–2008/09/08 2006/06/03–2009/07/27 2006/06/03–2009/09/11 2006/10/19–2009/07/27 2008/06/08–2007/09/06	
2007/09/06-2010/07/30 2007/10/22-2009/10/27 2008/09/08-2009/07/27 2009/09/11-2010/07/30	2007/10/22-2009/07/27 2008/06/08-2010/07/30 2008/10/24-2009/07/27 2009/10/27-2009/07/27 2009/10/27-2010/07/30	

Table 3
Interferograms used for estimating the average seasonal deformation between early June, late July, early September, and late October.

early June - late July	late July - early Sept.	early Sept late Oct.
2006/06/03-2009/07/27	2009/07/27-2007/09/06	2007/09/06-2007/10/22
2006/06/03-2010/07/30	2009/07/27-2008/09/08	2007/09/06-2008/10/24
2008/06/08-2009/07/27	2009/07/27-2009/09/11	2007/09/06-2009/10/27
2008/06/08-2010/07/30	2010/07/30-2007/09/06	2008/09/08-2008/10/24
	2010/07/30-2009/09/11	2008/09/08-2009/10/27
		2009/09/11-2007/10/22
		2009/09/11-2008/10/24
		2009/09/11-2009/10/27

#### 2007/09/06-2009/07/27 pair).

Because a strong long-term trend may mask the seasonal deformation signal, we only focused on the scenario where the active layer water storage remains unchanged over multiple years (Fig. 3 (b)) in the seasonal deformation analysis. We averaged all interferograms that include one SAR scene acquired in early June or late October, and another SAR scene acquired in late July or early September (Table 2 (right); after excluding all pixels with non-trivial long-term trends). We note that this seasonal stack solution underestimates the maximum seasonal subsidence, because (1) the active layer is not completely frozen by the end of October, and (2) a small frost heave may occur in early September at some locations during the ALOS PALSAR acquisition times (Section 5.2).

Similarly, we estimated the subsidence and uplift signatures due to the seasonal active layer FT processes between (i) early June and late July, (ii) late July and early September, and (iii) early September and late October by averaging all interferograms that span these periods as listed in Table 3. The early June to late July solution is a good approximation of the maximum seasonal subsidence, because late summer thaw in low porosity soils typically does not cause substantial thaw subsidence (Supplementary Materials S1).

Note that we can also compute seasonal deformation over other time intervals. For example, by averaging all interferograms that span late July and late October (*Supplementary Materials S3*), we can compute the average frost heave that occurred between late July and late October. Alternatively, we can combine the late July and early September stack solution with the early September and late October stack solution (Section 4.1) to derive a comparable seasonal surface deformation solution that occurred between late July and late October.

### 3.2.3. InSAR measurement uncertainty

The measured InSAR phase  $\Delta \varphi$  can be written as (Zebker and Villasenor, 1992; Zebker et al., 1994; Zebker et al., 1997):

$$\Delta \varphi = \frac{4\pi}{\lambda} \Delta d_{\text{LOS}} + \Delta \varphi_{dem} + \Delta \varphi_{alm} + \Delta \varphi_{lono} + \Delta \varphi_{orb} + \Delta \varphi_{decor} + \Delta \varphi_{unwrp} + \Delta \varphi_{n}$$
(6)

where  $\lambda$  is the radar wavelength, and  $\Delta d_{\rm LOS}$  is the LOS surface deformation between two SAR data acquisition times. The remaining phase terms on the right-hand side are errors due to inaccurate DEM ( $\Delta \phi_{dem}$ ), atmospheric ( $\Delta \phi_{atm}$ ) and ionospheric ( $\Delta \phi_{iono}$ ) artifacts, orbital errors ( $\Delta \phi_{orb}$ ), phase decorrelation ( $\Delta \phi_{decor}$ ) and phase unwrapping errors ( $\Delta \phi_{umwrp}$ ), and other error terms associated with thermal and soil moisture effects ( $\Delta \phi_n$ ).

Following the InSAR data processing strategy as described in Section 3.2.1, interferograms that contain large ionospheric errors were excluded in the analysis, and orbital errors were removed as a planar phase ramp.  $\Delta \phi_{decor}$  and  $\Delta \phi_{unwp}$  are associated with significant changes in surface scattering properties (e.g. vegetation growth) or phase ambiguity at isolated fast moving pixels (e.g. > 6 cm LOS motion between two adjacent pixels in a L-band interferogram). We excluded 8 interferograms that contain visible decorrelation and phase unwrapping artifacts (e.g., due to vegetation growth or other factors that change the surface scattering properties).  $\Delta \phi_{decor}$  and  $\Delta \phi_{unwp}$  in the remaining 58

interferograms were negligible.  $\Delta \varphi_n$  is typically at least an order magnitude smaller than the other error terms (Hanssen, 2001; Michaelides et al., 2019b). Hence we focused on evaluating the impact of DEM errors and tropospheric delays on the Toolik ALOS interferograms.

In Supplementary Materials S2, we show that ALOS pixels with large DEM errors are mostly located in rocky regions with steep terrain. Because of the lack of soil, these regions with exposed bedrock do not experience substantial seasonal deformation associated with the active layer freeze and thaw, and they are not the focus of this study. In addition, slope creep processes (e.g., Dini et al., 2019) may lead to a nonnegligible, long-term downward deformation trend in regions with large slope angles. We note that both DEM errors and slope creep signals are typically more noticeable in the long-term trend solution than in the seasonal deformation solution. Our analysis only focused on InSAR pixels without a detectable long-term deformation trend, where slope creep signals or DEM errors are not substantial.

Because the tundra climate is characterized by cool to cold temperatures and generally dry conditions, the impact of tropospheric noise is expected to be moderate to low (Supplementary Materials S3). We averaged interferograms that contain the common signal of interest (Section 3.2.2) (Rouvet et al., 2019; Sandwell and Price, 1998; Peltzer et al., 2001; Lyons and Sandwell, 2003). This can reduce the random tropospheric noise level by a factor of  $\sim \sqrt{N}$ , where N is the total number of SAR scenes used for generating the interferogram stack (Emardson et al., 2003). Under the assumption of a 2 cm tropospheric error across a single ALOS PLASAR interferogram (Zebker et al., 1997; Emardson et al., 2003), the tropospheric noise in the stack solutions is  $\sim 1$  cm or less. Furthermore, we compared the InSAR-observed deformation signals with the expected seasonal thaw subsidence calculated from field observations (Section 3.3). This allows us to confirm that the observed centimeter-level seasonal deformation patterns (in the regions where slope creep processes and DEM errors are not substantial) are indeed related to the freeze-thaw cycle of the active layer rather than residual tropospheric artifacts.

### 3.3. In-situ measurements

We conducted two field campaigns to measure in-situ soil properties that contain relevant information on water holding capacity. The undisturbed tundra soils in most of the Arctic consist of three distinct layers from the top to bottom: the acrotelm, the catotelm, and the mineral soil (Fig. 4a–b). The acrotelm and catotelm are organic soil layers with relatively high porosity. The boundary between these two layers is defined by the transition from peat containing living plants (acrotelm) to peat containing older dead plant material (catotelm). The bottom layer contains soils made mostly of low porosity, wind-deposited mineral soils (i.e., loess). The expected summer thaw subsidence  $\Delta d$  can thus be written as:

$$\Delta d = \frac{\rho_w - \rho_i}{\rho_i} \sum_{i=1}^3 z_i s_i \phi_i \tag{7}$$

where  $z_i$ ,  $s_i$ , and  $\phi_i$  are the thicknesses, the average saturation and the

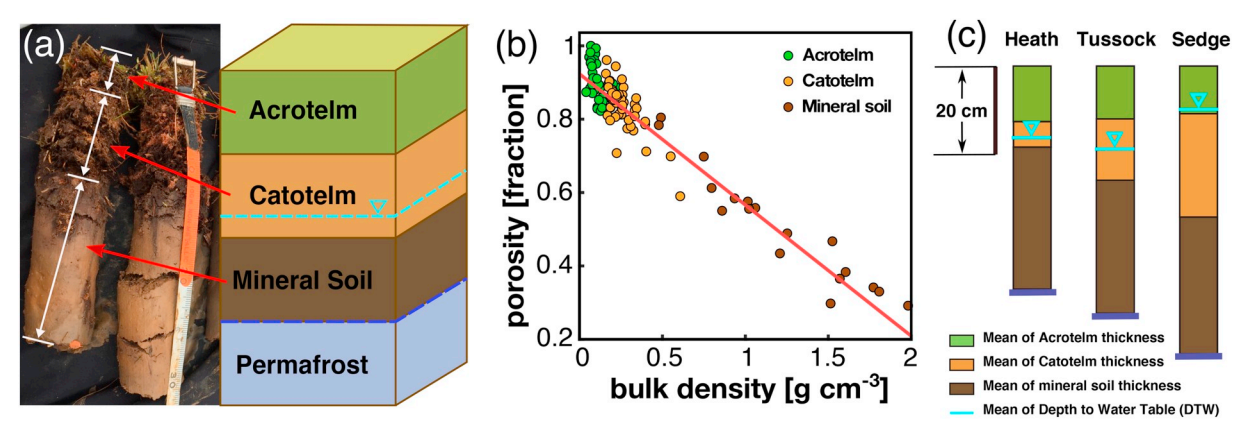


**Fig. 4.** (a) Soil core samples collected in 2018 near Toolik Lake. The tundra soils in the Toolik region consist of three distinct layers from the top to bottom: the acrotelm, the catotelm, and the mineral soil. The soil below the water table is considered as fully saturated (s = 1). (b) The porosity and bulk density measurements of soil samples collected from the acrotelm, the catotelm, and the mineral soil. In these soils the porosity typically decreases with the bulk density (data from O'Connor et al., 2020). (c) The average depth to the water table and soil layer thickness for heath, tussock and sedge land-cover types.

average porosity of the  $i^{th}$  thawed soil layer. We denote i=1 as the acrotelm layer, i=2 as the catotelm layer and i=3 as the mineral soil layer.

In 2018 (August 15–August 24) and 2019 (July 26–August 3), we collected 220 soil core samples at different sites near the Toolik Field Station (Fig. 1). Because our main focus is on the undisturbed permafrost landscape, we did not collect soil samples at remote sites such as the Anaktuvuk River fire scar. At each sample site, undisturbed soil samples from at least one soil layer were cored using a metal ring with a known volume (Fig. 5a). Porosity was determined by saturating the sample and then oven-drying, and the difference in weight provides the amount of water that can be held in the soil sample (Fig. 5b). For each soil pit we dug (Fig. 5c), we measured the depth of the acrotelm layer ( $z_1$ ) and the depth of the catotelm layer ( $z_2$ ) using a tape measure. We estimated the thaw depth ( $z_{\rm thaw}$ ) as the mean of five mechanical probing measurements near the soil pit (Brown et al., 2000). We calculated the depth of the mineral soil layer ( $z_3$ ) as  $z_{\rm thaw}-z_1-z_2$ . It is

reasonable to use in-situ thaw depth measurements collected between late July and late August to calculate  $\Delta d$  in Eq. (7). This is because mineral soils have much lower porosity and water holding capacity than do the shallower organic soil layers. As a result, a few centimeters of late summer thaw in August (Supplementary Materials S1) typically does not cause substantial thaw subsidence. For example, 5 cm thaw of the mineral soil layer with 47% porosity and 100% saturation only leads to  $\sim 2$  mm thaw subsidence, which is below the ALOS measurement noise level. The depth to the water table (DTW) was also measured at each site. Because the porosity in the acrotelm and catotelm layers is high ( $\sim 0.78$ –0.98) and water in the unsaturated zone can expand to cover the empty pore space during freezing without contributing to surface deformation, we ignored the soil water stored above the water table in the  $\Delta d$  calculation.

The amount of water in the active layer increases from hill ridges to valley bottoms, which influences the type of vegetation that can grow. Following this fact, we further divided the soil samples into soils

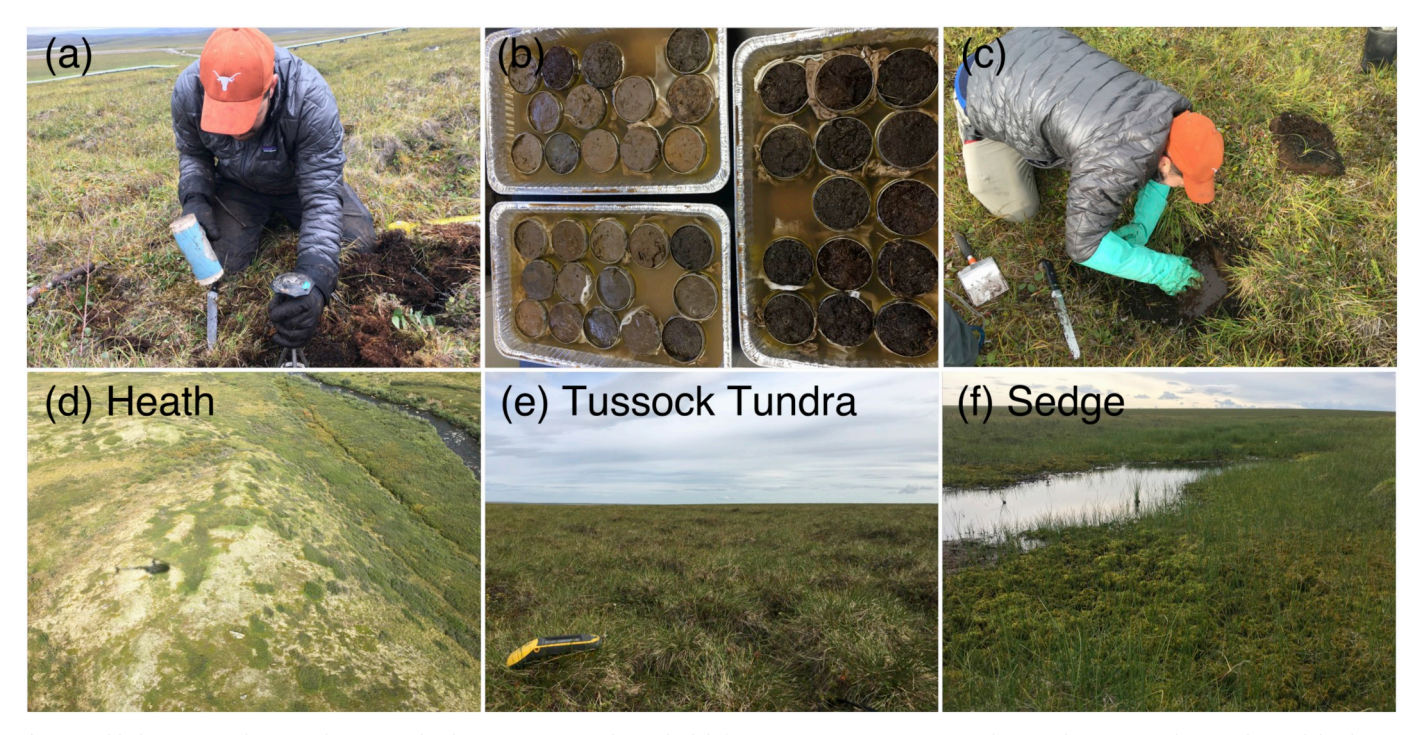


Fig. 5. Field photos. (a) Taking a soil core sample. (b) Saturating samples in the lab for measuring porosity. (c) A soil pit we dug at a sample site. (d) Heath land cover (e) Tussock Tundra land cover. (f) Wet sedge land cover.

underlying three general land cover types: heath vegetation (e.g., evergreen prostrate shrubs or other low-growing woody vegetation) on ridges, tussock tundra on hillslopes, and sedge vegetation in wetter or saturated valley bottoms (Fig. 4c and Fig. 5d–f). Note that certain water-loving shrubs (e.g., willow) often grow along water tracks. We did not analyze the woody vegetation along water tracks in this study, because the soils here typically only contain well-drained acrotelm and often gravel and boulders at depth. While we do not expect substantial seasonal deformation associated with the active layer freeze and thaw (due to the lack of saturated soil layers) at these water tracks, the movement of gravels may lead to surface motion that is not the focus of this study.

#### 4. Results

## 4.1. Long-term and seasonal deformation from InSAR observations

We observed a  $\sim 2-3$  cm/year subsidence trend between 2006 and 2010 over the southern-most portion of the 2007 Anaktuvuk River fire zone (highlighted by the dark green squares in Fig. 6a). Outside the fire zone, we observed  $\sim 0.6-1$  cm/year subsidence trend in some rocky regions with very steep terrain, which may be due to DEM errors or slope creep processes (*Supplementary Materials S2*). We did not observe any detectable trend at the majority of InSAR pixels shown in yellow in Fig. 6a). In the remainder of the paper, our discussions focus on those pixels, where the observed InSAR deformation signals are mainly related to the seasonal active layer freeze-thaw cycle (Fig. 6b).

Due to the lack of ALOS acquisitions in August, we observed the maximum seasonal thaw subsidence between early June and late July (Fig. 7a). We observed a net uplift between late July and early September (Fig. 7b) and between early September and late October (Fig. 7c). An important finding from this study is that the observed seasonal thaw subsidence and frost heave patterns are related to the local topography as well as the local watershed and river network morphology (Fig. 8). The smaller seasonal deformation (~ 2 cm or less) is often observed at the hill ridges where the soil is the least saturated, and the larger seasonal deformation (~ 3 cm or more) is mostly observed in the river valleys where the soil is typically fully saturated. We note that the maximum seasonal thaw subsidence is proportional to the active layer soil water content as described in Section 3.1, and topography is one of many factors that influence soil water distributions.

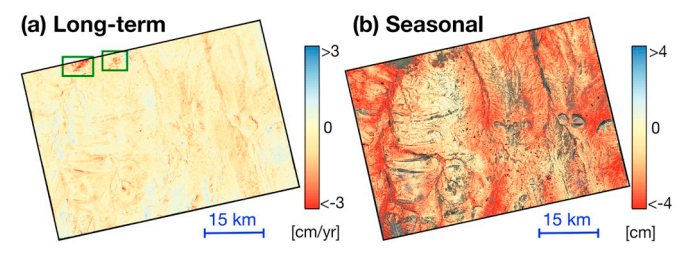


Fig. 6. (a) InSAR-observed long-term surface deformation trend (cm/year) between 2006 and 2010 over the Toolik area. Here red means subsidence, yellow means no significant deformation, and blue means uplift. The 2007 Anaktuvuk River fire resulted in a detectable long-term subsidence trend ( $\sim$  2 cm/year-3 cm/year) in regions highlighted by the dark green squares. The ALOS spatial coverage over the area of interest ( $\sim$  65 km  $\times$  45 km) is outlined in green in Fig. 1. (b) InSAR-observed average seasonal thaw subsidence (cm) between 2006 and 2010 over the same area. We masked-out pixels with a long-term subsidence trend greater than 6 mm/year, because DEM errors or slope creep processes may contribute to the observed deformation signals at those pixels. (For interpretation of the references to colour in this figure legend, the reader is referred to the web version of this article.)

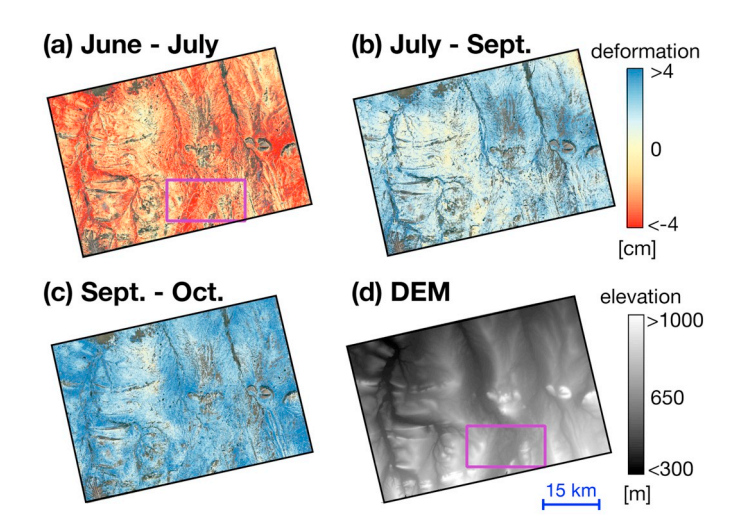


Fig. 7. Average surface deformation between (a) early June and late July, (b) late July and early September, and (c) early September and late October. Here red means subsidence, yellow means no significant deformation, and blue means uplift. We masked-out pixels with a long-term subsidence trend greater than 6 mm/year, because DEM errors or slope creep processes may contribute to the observed deformation signals at those pixels. (d) The Digital Elevation Model (DEM) in the Toolik area. The spatial coverage over the area of interest ( $\sim65~{\rm km}\times45~{\rm km})$  is outlined in green in Fig. 1. Note that the observed seasonal deformation pattern shows a strong correlation with the local topography as well as the local watershed and river network morphology. The regions outlined in purple are magnified in Fig. 8 for further comparison. (For interpretation of the references to colour in this figure legend, the reader is referred to the web version of this article.)

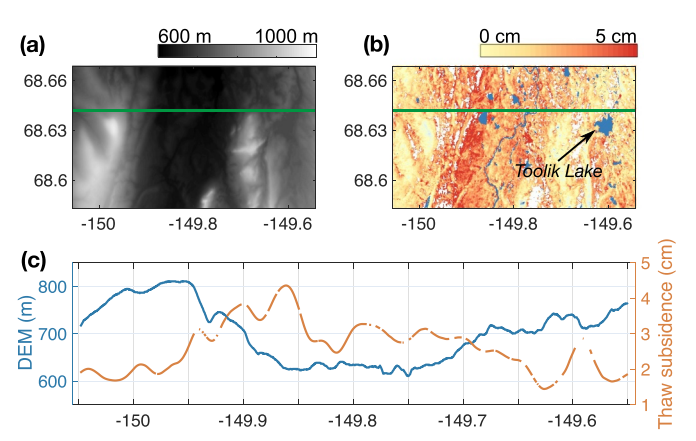


Fig. 8. (a) The Digital Elevation Model (DEM) over the area outlined in purple in Fig. 7 (d) on a latitude/longitude grid. (b) Average thaw subsidence between early June and late July (2006–2010) over the area outlined in purple in Fig. 7 (a). Water pixels are marked in blue. We masked-out pixels with a long-term subsidence trend greater than 6 mm/year, because DEM errors or slope creep processes may contribute to the observed deformation signals at those pixels. (c) The DEM and June–July thaw subsidence profiles along the green transect marked in panels (a) and (b). A Gaussian filter was applied to the June–July subsidence profile to match the spatial resolution of DEM data. We note that the maximum seasonal thaw subsidence is proportional to the active layer soil water content as described in Section 3.1, and topography is one of many factors that influence soil water distributions. (For interpretation of the references to colour in this figure legend, the reader is referred to the web version of this article.)

## 4.2. Comparison between InSAR and in-situ observations

A direct comparison between remotely-sensed measurements and field measurements is often impossible because they cover very different temporal and spatial scales. While the spatial resolution of InSAR

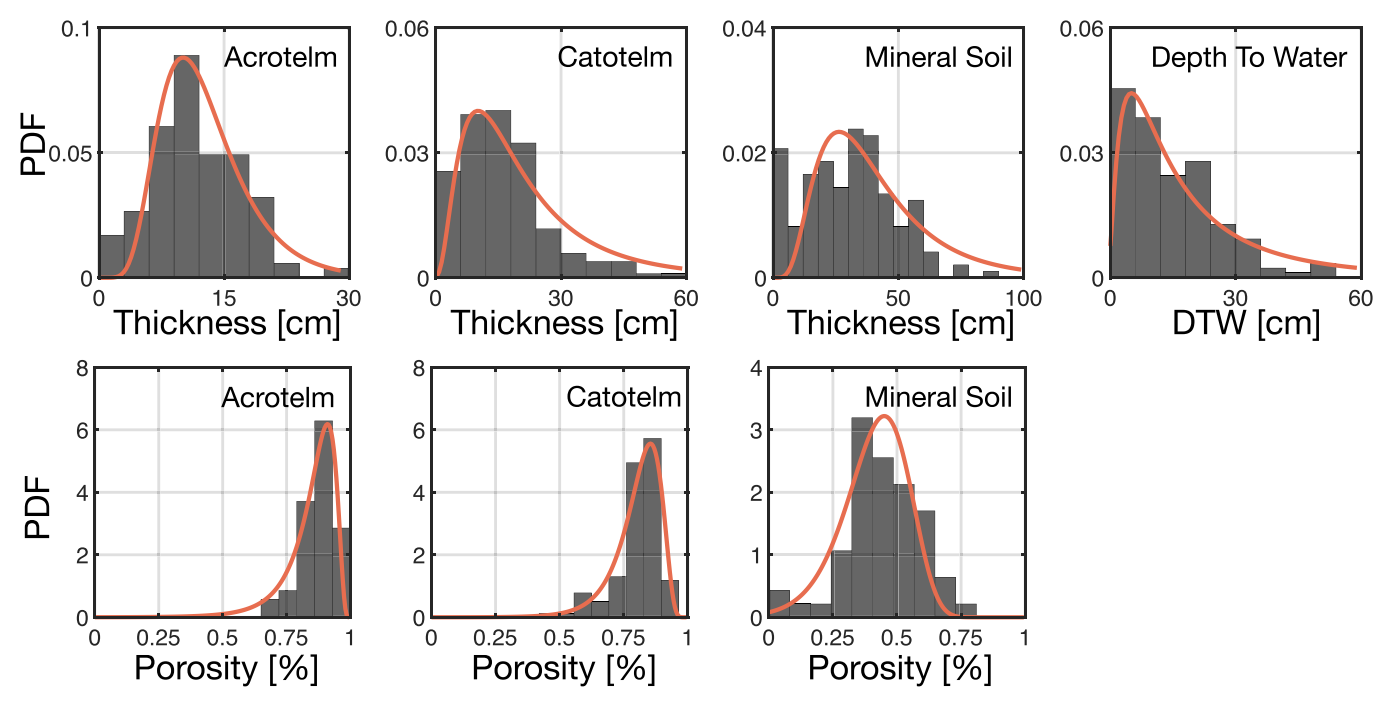


Fig. 9. Acrotelm, catotelm, and mineral layer thickness (cm) and porosity (%), and the depth to the water table (cm) distributions as inferred from field and lab measurements. We fitted each distribution with a log-normal probability density function (in red). (For interpretation of the references to colour in this figure legend, the reader is referred to the web version of this article.)

deformation maps is on the order of 10s-100s of meters, in-situ measurements can vary significantly due to the sub-meter-scale heterogeneity of arctic soils. To characterize the range and variance in soil properties, we collected and analyzed a large number of in-situ measurements that contain relevant information on water holding capacity as described in Section 3.3. We fitted a log-normal probability density function (PDF) to the distribution of each soil property (Fig. 9). We then drew random samples from these PDFs, and computed the distribution of the equivalent water depth ( $z_{water}$ ) based on Eq. (7) through  $10^5$ Monte Carlo simulations. Following Eq. (2), 75% of the Monte Carlo simulations suggest a  $z_{\rm water}$  value less than 44.5 cm (4 cm thaw subsidence), and the median  $z_{\rm water}$  equals 30.7 cm (2.8 cm thaw subsidence) (Fig. 10a). On the other hand, the median thaw subsidence measurements of all InSAR pixels equals 2.6 cm, which suggests an  $z_{water}$  of 28.8 cm (Fig. 10b). InSAR thaw subsidence observations have a smaller standard deviation than the estimated thaw subsidence from the Monte Carlo simulations (Fig. 10c). This is because (1) the uncertainty of field measurements is larger due to the sub-meter-scale heterogeneity of arctic soils, and (2) InSAR and in-situ measurements have different sampling frequencies for different land cover types.

Because the availability of water influences the type of vegetation that can grow, we found that InSAR-observed deformation patterns are in agreement with land vegetation cover types along a geomorphic-ecohydrologic transect with heath and some tussock vegetation on ridges, tussock tundra on hillslopes, and sedge tundra and occasional shrubs on higher ground (mounds) at the valley-bottom riparian zone. We grouped in-situ soil samples collected under dry heath vegetation, tussock tundra, and sedge tundra (Table 4), and simulated the expected seasonal thaw subsidence for each land cover (Fig. 11a). The median thaw subsidence values for these three vegetation covers are 1.5 cm, 2.0 cm, and 2.9 cm, respectively, based on the Monte Carlo simulations. This means that on average, sedges grow in soils than contain ~ 30% more water than in tussocks and ~ 50% more water than in heaths.

Using the North Slope Science Initiative (NSSI) Landcover GIS Data, we selected sedge tundra, tussock tundra, and woody shrub InSAR pixels along a ridge-to-ridge transect (Fig. 11b-d). The median

June–July thaw subsidence is 3 cm for 3157 sedge tundra pixels, and 2.2 cm for 7683 tussock tundra pixels. More specifically, 49.3% of the sedge tundra pixels and 25.3% of the tussock tundra pixels show more than 3 cm of thaw subsidence, while 23.7% of the sedge pixels and 39.4% of the tussock tundra pixels display less than 2 cm of thaw subsidence. While InSAR and in-situ observations show good agreement for tussock and sedge vegetation covers, the Monte Carlo simulations for heath vegetation show lower values than the 1532 InSAR woody shrub pixels. This is because we cannot distinguish woody shrubs that grow on drier hill ridges (e.g., heath) and wetter or saturated water tracks (e.g., willows and birch) using the NSSI woody shrub classification data. In addition, different varieties of dwarf shrubs may grow all over the place, which can add to the complexity in sub-classifications of woody vegetation.

#### 5. Discussion

## 5.1. InSAR observations and the active layer thickness (ALT)

As discussed in Section 3.1, if the net water drainage is minimal  $(P - ET - Q \approx 0)$ , then only thaw deepening at the bottom of the active layer into permafrost with non-negligible ice content can increase the maximum seasonal thaw subsidence. Michaelides et al., 2019a in a recent permafrost wildfire study noted that the InSAR-observed deformation patterns are related to the temporal recovery of the vegetation within the fire zone. They found that the removal of vegetation and organic materials by fire increases energy absorption by the ground, which leads to an increase in ALT and seasonal thaw subsidence over multiple FT cycles. This is likely the cause of the observed long-term subsidence trend in the 2007 Anaktuvuk River fire zone. Outside the fire zone, while we observed detectable centimeter-level deformation associated with the active layer seasonal freeze and thaw processes, we did not observe any long-term subsidence trend above the noise level (~ 5 mm/year). This suggests that the maximum seasonal thaw depth was stable between 2006 and 2010, or thaw deepening did not cause any detectable increase in the active layer soil water content

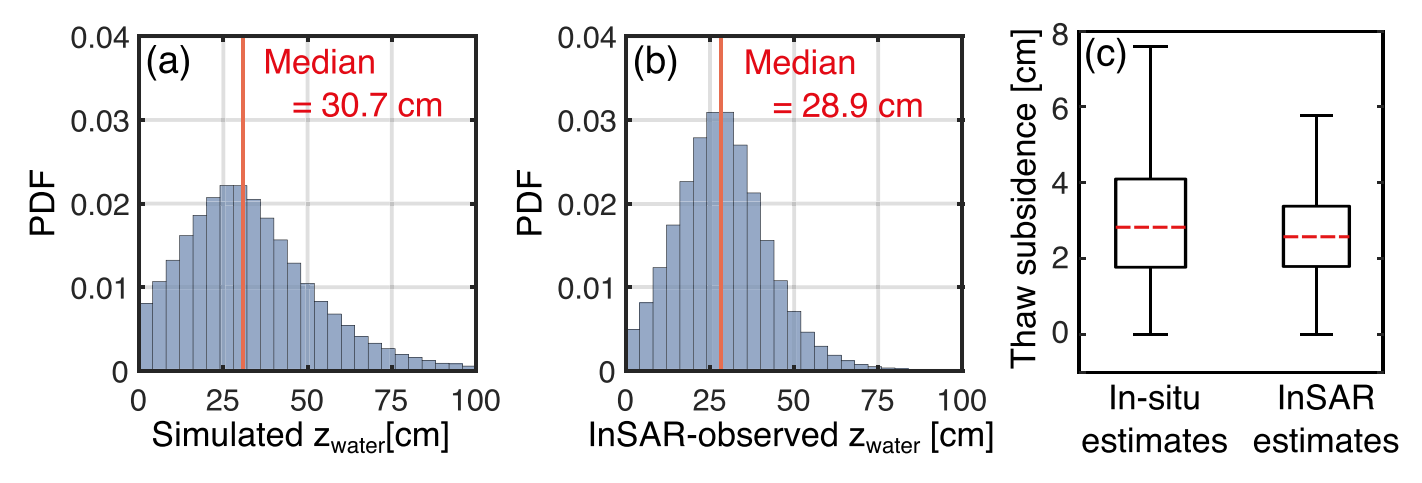


Fig. 10. The equivalent water depth  $z_{\rm water}$  (cm) distribution as derived from (a)  $10^5$  Monte Carlo simulations that are constrained by in-situ measurements, and (b) InSAR observations at all pixel locations. (c) Thaw subsidence between early June and late July as estimated from both in-situ and InSAR observations. When a 10.9 cm solid ice column thaws, it becomes a 10 cm liquid water column. The median thaw subsidence of all Monte Carlo simulations is 2.8 cm, and the median value of all InSAR pixels is 2.6 cm.

**Table 4** Mean and standard deviation of the depth to the water table (DTW), and the thickness of the acrotelm  $(d_1)$ , catotelm  $(d_2)$ , and mineral soil  $(d_3)$  layers as derived from 220 Toolik soil core samples for three general land cover types.

	DTW (cm)	$d_1$ (cm)	$d_2$ (cm)	<i>d</i> <sub>3</sub> (cm)
Heath	15.5 ± 6.5	$12.0 \pm 6.5$ $11.4 \pm 5.2$ $10.2 \pm 5.6$	5.2 ± 4.6	31.7 ± 18.3
Tussock Tundra	18.1 ± 13.7		13.3 ± 8.9	29.6 ± 16.3
Sedge Tundra	9.1 ± 9.8		22.9 ± 14.1	30.5 ± 21.3

in the undisturbed study area (under the assumption  $P-ET-Q\approx 0$ ). In-situ thaw depth measurements (Fig. 12) show that the August 11 thaw depth ( $\sim$  40 cm) at the Toolik grid has increased very slightly since 1990. At the Imnavait grid, the August 11 thaw depth increase between 2006 and 2010 is  $\sim$  5 cm. As discussed in Section 3.3, 5 cm thaw of the low porosity mineral soils was unlikely to cause any soil water content increase that is detectable by InSAR. Here we want to emphasize that the presence of a long-term subsidence trend indicates an increase in the active layer soil water content, and the active layer thickness is not the only factor that influences the soil water content. Additional information on the depth of the water table as well as how soil porosity changes with depth is required to retrieve the absolute ALT from InSAR observations.

## 5.2. InSAR observations and the active layer freeze-thaw dynamics

Daout et al., 2017 showed that the onset of frost heave was earlier in regions that experienced larger seasonal thaw subsidence using Tibetan InSAR observations. Our InSAR results are consistent with this findings. A net uplift was observed between late July and early September in the Toolik area, mostly in the wetter riparian zone that experienced a larger seasonal thaw subsidence. Toolik Field Station in-situ data (Fig. 13a) suggest that the air temperature fluctuated around or below freezing in early September during the ALOS PALSAR data acquisition times (at ~ 12 am local time on 2007/09/06, 2008/09/08, and 2009/09/11). In this scenario, ice can be formed at the top of the soil, which leads to frost heave in saturated soils. We do not expect to detect frost heave in drier unsaturated soils, because water in the unsaturated zone can expand to cover the empty pore space during freezing without contributing to heave. Additional frost heaving was observed between early September and late October at all pixels that experienced thaw subsidence in the summer thaw season. The total thaw subsidence that occurred between early June and late July is larger than the total frost heave that occurred between late July and late October. This suggests that frost heave continued after late October until the active layer was completely frozen in November–December.

In contrast, previous studies (Liu et al., 2012; Schaefer et al., 2015) assumed that the InSAR-observed thaw subsidence is proportional to the square root of the normalized Accumulated Degree Days of Thaw (ADDT; defined as the total number of days with average daily air temperatures above 0 degree Celsius), and that the maximum subsidence occurs on or after the surface temperature returns to freezing. Based on the Toolik ADDT curve (Fig. 13b), the onset of thaw subsidence was expected to occur in early June (~ the 150th days of the year) and the maximum thaw subsidence was expected to occur after mid-September ( $\sim$  the 260<sup>th</sup> days of the year). The possible reasons that ALOS data detected an earlier onset of frost heaving than the ADDT model are as follows: (1) ALOS PALSAR satellite acquired data at midnight when the air temperature was close to the daily minimum rather than the daily average; and (2) the air temperature is not the only factor that controls the active layer FT dynamics. As discussed in Section 3.2.2, thermal diffusivity and thickness of soil columns can also play a role. Moreover, 1 cm of thaw often does not result in the same amount of thaw subsidence. This is because the water holding capacity of soils varies at different locations and depths.

#### 6. Conclusion

In this study we analyzed 12 ALOS PALSAR scenes (2006-2010) and 220 soil core samples collected at various sites within  $\sim 100$  km of the Toolik Field Station. This allowed us to show that the amplitude of the seasonal thaw subsidence is proportional to the total amount of water that freezes and thaws annually, but not necessarily to the ALT. Our InSAR results reveal that the observed deformation patterns are mainly related to soil water content and the seasonal active layer freeze-thaw cycle, and no substantial long-term subsidence trend was observed outside the 2007 Anaktuvuk River Fire scar. We found that the onset of frost heave occurred in early September, when the temperature fluctuated around freezing. In this scenario, ice can be formed at the top of the soil, which leads to frost heave in saturated soils. We also found that InSAR-observed seasonal deformation patterns are related to land cover (vegetation) types. The deformation amplitude increases along a geomorphic-ecohydrologic transect with heath and some tussock vegetation on ridges, tussock tundra on hillslopes, and sedge tundra and occasional shrubs on higher ground (mounds) in the valley-bottom riparian zone. Our results demonstrate that satellite geodetic data can

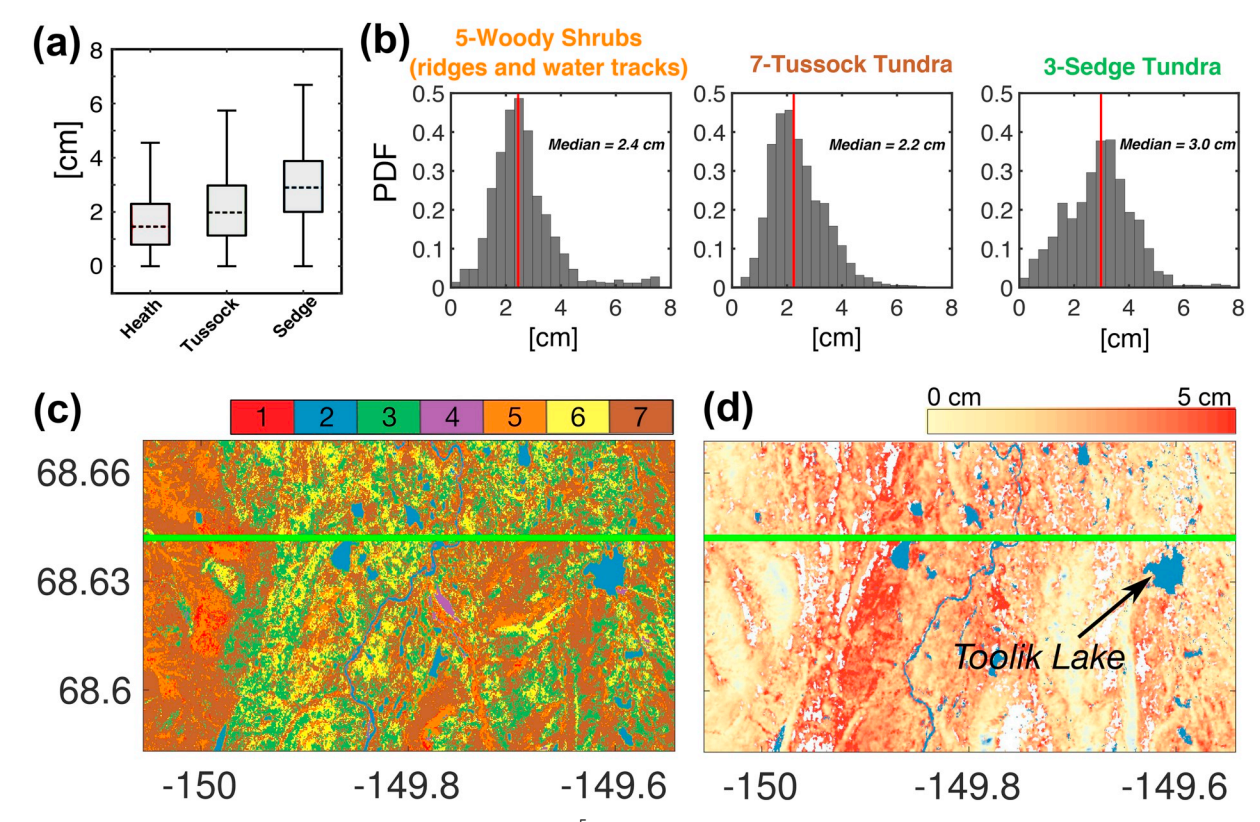


Fig. 11. (a) The expected seasonal thaw subsidence as derived from  $10^5$  Monte Carlo simulations that are constrained by in-situ measurements. The median subsidence values for heath, tussock tundra and sedge tundra are 1.5 cm, 2.0 cm, and 2.9 cm. (b) The distributions of the InSAR thaw subsidence measurements for woody shrubs (including woody vegetation on ridges and near water tracks), tussock tundra, and sedge tundra along the green transect marked in panel (d). Red lines show median values. (c) North Slope Science Initiative (NSSI) land cover GIS Data (1-Alder, 2-Water, 3-Sedge Tundra, 4-Bare Land, 5-Woody Shrub, 6-Dwarf Shrub, 7-Tussock Tundra) over the area outlined in purple in Fig. 7(a) on a latitude/longitude grid. We collected soil samples under heath (upland woody shrubs), tussock, and sedge land covers. Note that certain water-loving shrubs (e.g., willow) often grow along water tracks, and we did not analyze these water track woody samples. (d) Mean thaw subsidence between early June and late July (2006–2010) over the same region. Water pixels are marked in blue. We masked-out pixels with a long-term subsidence trend greater than 6 mm/year, because DEM errors or slope creep processes may contribute to the observed deformation signals at those pixels. (For interpretation of the references to colour in this figure legend, the reader is referred to the web version of this article.)

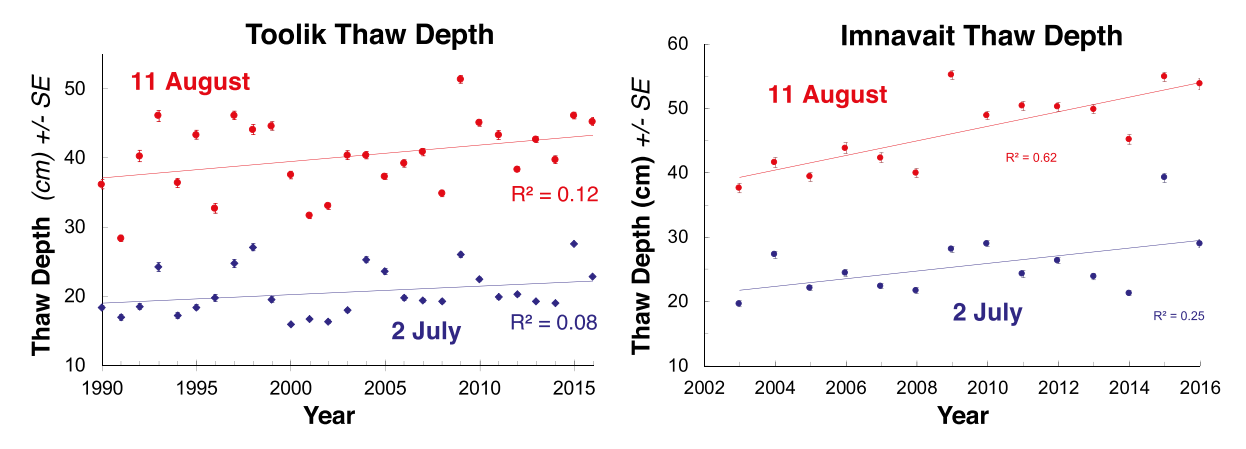


Fig. 12. Probing thaw depth measurements on 2 July and 11 August (~ max thaw) for the Toolik Lake (1990–2016) and Imnavait Creek (2003–2016) thaw measurement grids (data source: Arctic Long Term Ecological Research (Arctic LTER) program; see also Hobbie and Kling, 2014. The locations of the thaw grids are illustrated in Fig. 1.

fill a critical gap in the current arctic hydrology observing system, which can help us to better understand the hydrologic dynamics in thawing permafrost.

We note that the ALOS PALSAR data that were employed in this study have a limited temporal sampling rate. As a result, we could only derive seasonal deformation that occurred between early June, late July, early September, and late October. No ALOS acquisition was made over this area in August when the annual thaw depth is expected to

reach the maximum. In addition, we were unable to distinguish the variability in the active layer water storage from year to year, because the stacking approach assumes that the InSAR deformation signals associated with the active layer freeze and thaw over multiple FT cycles are identical. Recently launched satellite missions such as Sentinel-1 have provided nearly global InSAR data coverage on a 6-day repeat cycle with a two-satellite constellation. Scheduled for launch in 2022, the NASA-ISRO Synthetic Aperture Radar (NISAR) mission will

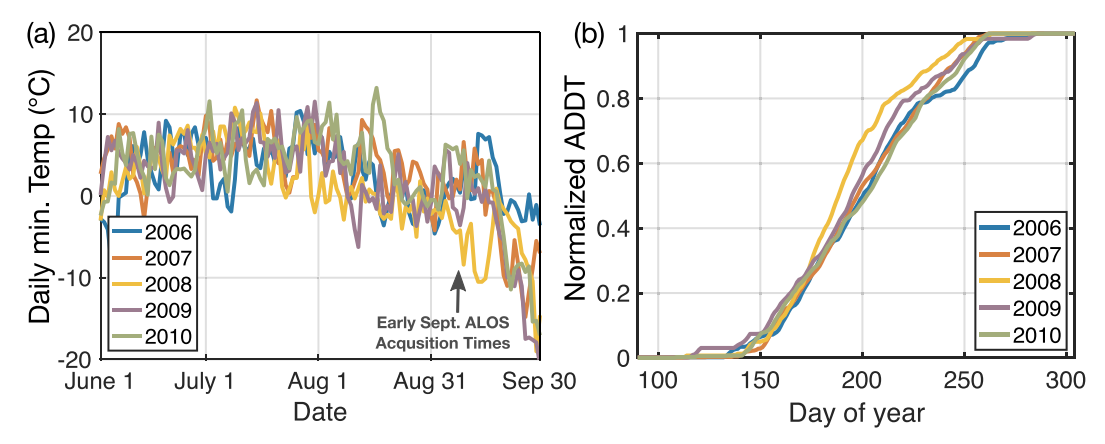


Fig. 13. (a) Toolik Field Station daily minimum air temperature measurements at 5 m height between June and September (2006–2010). The Toolik ALOS early September scenes were acquired at 8:00 UTC (at 12 am local time during daylight savings) on 2007/09/06, 2008/09/08, and 2009/09/11 when the air temperature fluctuated around or below freezing. (b) Normalized Accumulated Degree Days of Thaw (ADDT) curve (2006–2010) at the Toolik Field Station. Here we calculated daily ADDT as the total number of days with average daily air temperatures above 0 degree Celsius. We normalized the ADDT curve by the total number of degree days of thaw for a given year.

continue to measure surface deformation with a sampling interval of 12 days and resolution of 100 m over at least 70% of the specified regions of Earth's land surface. The broad spatial and temporal coverage of the current and next generations of InSAR data can be potentially used to refine our understanding of the dynamics and hydrological state of permafrost at a pan-arctic scale.

#### **Author contributions**

Conceptualization: K. Schaefer originally conceived conducting InSAR in the Toolik area. The project was designed by J. Chen with contributions from M. Cardenas and G. Kling. Methodology, J. Chen, M.B. Cardenas and G. Kling; InSAR data analysis, J. Chen and Y. Wu; Field data collection and analysis, Y. Wu and M. O'Connor; Writing–original draft preparation, J. Chen; Writing–review and editing, all authors; Visualization, Y. Wu. and J. Chen; Funding acquisition, J. Chen, M.B. Cardenas, G. Kling and K. Schaefer.

## **Declaration of Competing Interest**

None

## Acknowledgments

This research was funded by the NASA Terrestrial Hydrology Program, grant 80NSSC18K0983 to J. Chen, M.B. Cardenas and G. Kling and and NSF grants PLR 1504006 and DEB 1637459. K. Schaefer was supported by NASA Grants NNX16AH36A, NNX13AM25G, NNX17AC59A, and NSF grant ARC 1204167. R. Michaelides was supported by NASA grant NNX16AH36A and NSF GRFP Grant DGE 1656518

Arctic DEM data were provided by the Polar Geospatial Center at https://www.pgc.umn.edu/data/arcticdem/. Kuparuk River watershed DEM data were obtained at https://toolik.alaska.edu/gis/data/index.php. ALOS PALSAR data were downloaded from from the Alaska Satellite Facility at https://ursa.asfdaac.alaska.edu/. North Slope Science Initiative (NSSI) Landcover GIS Data were downloaded from http://catalog.northslopescience.org. Toolik Field Station air temperature data were downloaded from https://toolik.alaska.edu/edc. Toolik in-situ soil measurements collected in the 2018 and 2019 summer field campaigns can be accessed from O'Connor et al., 2020.

The authors would like to thank Jason Dobkowski for thaw probe measurements and analyses and three anonymous reviewers who provide constructive feedback that improves the quality of this paper.

#### Appendix A. Suplementary information

#### References

Alexander, R.B., Boyer, E.W., Smith, R.A., Schwarz, G.E., Moore, R.B., 2007. The role of headwater streams in downstream water quality. JAWRA 43 (1), 41–59.

Antonova, S., Kb, A., Heim, B., Langer, M., Boike, J., 2016. Spatio-temporal variability of x-band radar backscatter and coherence over the lena river delta, siberia. Remote Sens. Environ. 182, 169–191. https://doi.org/10.1016/j.rse.2016.05.003.

Antonova, S., Sudhaus, H., Strozzi, T., Zwieback, S., Kaab, A., Heim, B., Langer, M., Bornemann, N., Boike, J., 2018. Thaw subsidence of a yedoma landscape in northern siberia, measured in situ and estimated from terrasar-x interferometry. Remote Sens 10 (4). https://doi.org/10.3390/rs10040494.

Aufdenkampe, A.K., Mayorga, E., Raymond, P.A., Melack, J.M., Doney, S.C., Alin, S.R., Aalto, R.E., Yoo, K., 2011. Riverine coupling of biogeochemical cycles between land, oceans, and atmosphere. Front. Ecol. Environ. 9 (1), 53–60. https://doi.org/10.1890/100014.

Bartsch, A., Widhalm, B., Leibman, M., Ermokhina, K., Kumpula, T., Skarin, A., Wilcox, E.J., Jones, B.M., Frost, G.V., Hfler, A., Pointner, G., 2020. Feasibility of tundra vegetation height retrieval from sentinel-1 and sentinel-2 data. Remote Sensing Environ. 237, 111515. https://doi.org/10.1016/j.rse.2019.111515.

Battin, T.J., Kaplan, L.A., Findlay, S., Hopkinson, C.S., Marti, E., Packman, A.I., Newbold, J.D., Sabater, F., 2009. Biophysical controls on organic carbon fluxes in fluvial networks. Nat. Geosci. 1, 95–100. https://doi.org/10.1038/ngeo101.

Brown, J., Hinkel, K.M., Nelson, F.E., 2000. The circumpolar active layer monitoring (calm) program: research designs and initial results. Polar Geogr. 24 (3), 166–258. https://doi.org/10.1080/10889370009377698.

Chen, C.W., Zebker, H.A., 2001. Two-dimensional phase unwrapping with use of statistical models for cost functions in nonlinear optimization. J. Opt. Soc. Am. A 18 (2), 338–351. https://doi.org/10.1364/JOSAA.18.000338.

Chen, R.H., Tabatabaeenejad, A., Moghaddam, M., 2019. Retrieval of permafrost active layer properties using time-series p-band radar observations. IEEE Trans. Geosci. Remote Sens. 57 (8), 6037–6054.

Cole, J.J., Caraco, N.F., Kling, G.W., Kratz, T.K., 1994. Carbon dioxide supersaturation in the surface waters of lakes. Science 265 (5178), 1568–1570. https://doi.org/10. 1126/science.265.5178.1568.

Daout, S., Doin, M.-P., Peltzer, G., Socquet, A., Lasserre, C., 2017. Large-scale InSAR monitoring of permafrost freeze-thaw cycles on the Tibetan Plateau. Geophys. Res. Lett. 44 (2), 901–909. https://doi.org/10.1002/2016GL070781.

Dini, B., Daout, S., Manconi, A., Loew, S., 2019. Classification of slope processes based on multitemporal dinsar analyses in the himalaya of nw Bhutan. Remote Sens. Environ. 233, 111408. https://doi.org/10.1016/j.rse.2019.111408.

Emardson, T.R., Simons, M., Webb, 2003. Neutral atmospheric delay in interferometric synthetic aperture radar applications: Statistical description and mitigation. J. Geophys. Res. 108, 2231.

Fattahi, H., Simons, M., Agram, P., 2017. InSAR time-series estimation of the ionospheric phase delay: an extension of the split range-spectrum technique. IEEE Trans. Geosci. Remote Sensing 1–13. https://doi.org/10.1109/TGRS.2017.2718566.

Fisher, J., Hayes, D., Schwalm, C., Huntzinger, D., Stofferahn, E., Schaefer, K., Luo, Y., Wullschleger, S., Goetz, S., Miller, C., Griffith, P., Chadburn, S., Chatterjee, A., Ciais, P., Douglas, T., Genet, H., Ito, A., Neigh, C., Poulter, B., Rogers, B., Sonnentag, O., Tian, H., Wang, W., Xue, Y., Yang, Z., Zeng, N., Zhang, Z., 2018. Missing pieces to modeling the arctic-boreal puzzle. Environ. Res. Lett. 13 (2). https://doi.org/10.

- 1088/1748-9326/aa9d9a.
- Hamilton, T.D., 1975. Itkillik glaciation in the Brooks Range, northern Alaska. Quat. Res. 5, 471–497. https://doi.org/10.1016/0033-5894(75)90012-5.
- Hamilton, T., 1986. Late Cenozoic Glaciation of the Central Brooks Range, Glaciation in Alaska: The Geologic Record. Alaska Geological Society, Anchorage, pp. 9–49.
- Hanssen, R., 2001. Radar Interferometry: Data Interpretation and Error Analysis, Remote Sensing and Digital Image Processing. Springer.
- Hobbie, J., Kling, G., 2014. Alaska's Changing Arctic: Ecological Consequences for Tundra, Streams, and Lakes. https://doi.org/10.1093/acprof:osobl/9780199860401. 001 0001
- Iwahana, G., Uchida, M., Liu, L., Gong, W., Meyer, F.J., Guritz, R., Yamanokuchi, T., Hinzman, L., 2016. InSAR detection and field evidence for thermokarst after a tundra wildfire, using ALOS-PALSAR. Remote Sens 8 (3). https://doi.org/10.3390/ rs8030218
- Jorgenson, M.T., Shur, Y.L., Pullman, E.R., 2006. Abrupt increase in permafrost degradation in Arctic Alaska. Geophys. Res. Lett. 33 (2). https://doi.org/10.1029/2005GL024960.
- Kling, G., Kipphut, G., Miller, M., 1991. Arctic lakes and streams as gas conduits to the atmosphere: implications for tundra carbon budgets. Science (New York, N.Y.) 251, 298–301. https://doi.org/10.1126/science.251.4991.298.
- Liu, L., Jafarov, E.E., Schaefer, K.M., Jones, B.M., Zebker, H.A., Williams, C.A., Rogan, J., Zhang, T., 2014. InSAR detects increase in surface subsidence caused by an Arctic tundra fire. Geophys. Res. Lett. 41 (11), 3906–3913. https://doi.org/10.1002/ 2014GI.060533.
- Liu, L., Schaefer, K.M., Chen, A.C., Gusmeroli, A., Zebker, H.A., Zhang, T., 2015. Remote sensing measurements of thermokarst subsidence using InSAR. J. Geophys. Res. 120 (9), 1935–1948. https://doi.org/10.1002/2015JF003599.
- Liu, L., Zhang, T., Wahr, J., 2010. InSAR measurements of surface deformation over permafrost on the North Slope of Alaska. J. Geophys. Res. 115, F03023. https://doi. org/10.1029/2009JF001547.
- Lyons, S., and Sandwell, D., 2003, Fault creep along the southern San Andreas from interferometric synthetic aperture radar, permanent scatterers, and stacking, J. Geophys. Res., 108, 2047, doi:10.1029/2002JB001831, B1.
- L. Liu, K. Schaefer, T. Zhang, J. Wahr, 2012, Estimating 1992-2000 average active layer thickness on the Alaskan North Slope from remotely sensed surface subsidence, J. Geophys. Res. 117 (F1). doi:https://doi.org/10.1029/2011JF002041.
- Macdougall, A.H., Avis, C. A, Weaver, A., 2012. Significant contribution to climate warming from the permafrost carbon feedback. Nat. Geosci. 5. https://doi.org/10. 1038/NGF01573.
- McDonnell, J.J., 2003. Where does water go when it rains? Moving beyond the variable source area concept of rainfall-runoff response. Hydrol. Process. 17 (9), 1869–1875. https://doi.org/10.1002/hyp.5132.
- McGuire, A.D., Anderson, L.G., Christensen, T.R., Dallimore, S., Guo, L., Hayes, D.J., Heimann, M., Lorenson, T.D., Macdonald, R.W., Roulet, N., 2009. Sensitivity of the carbon cycle in the Arctic to climate change. Ecol. Monogr. 79 (4), 523–555. https:// doi.org/10.1890/08-2025.1.
- McNamara, J.P., Kane, D.L., Hinzman, L.D., 1998. An analysis of streamflow hydrology in the Kuparuk River Basin, Arctic Alaska: a nested watershed approach. J. Hydrol. 206 (1), 39–57. https://doi.org/10.1016/S0022-1694(98)00083-3.
- Michaelides, R.J., Schaefer, K., Zebker, H.A., Parsekian, A., Liu, L., Chen, J., Natali, S., Ludwig, S., Schaefer, S.R., 2019a. Inference of the impact of wildfire on permafrost and active layer thickness in a discontinuous permafrost region using the remotely sensed active layer thickness (ReSALT) algorithm. Environ. Res. Lett. 14 (3), 035007. https://doi.org/10.1088/1748-9326/aaf932.
- Michaelides, R., Zebker, H., Zheng, Y., 2019b. An algorithm for estimating and correcting decorrelation phase from Insar data using closure phase triplets. IEEE Trans. Geosci. Remote Sensing 1–8. https://doi.org/10.1109/TGRS.2019.2934362.
- Molan, Y.E., Kim, J.-W., Lu, Z., Wylie, B., Zhu, Z., 2018. Modeling wildfire-induced permafrost deformation in an Alaskan boreal forest using InSAR observations. Remote Sens 10 (3). https://doi.org/10.3390/rs10030405.
- Munroe, J.S., Bockheim, J., 2001. Soil development in low-arctic tundra of the northern Brooks Range, Alaska, U.S.A. Arct. Antarct. Alp. Res. 33, 78. https://doi.org/10. 2307/1552280.
- Neilson, B.T., Cardenas, M.B., O'Connor, M.T., Rasmussen, M.T., King, T.V., Kling, G.W., 2018. Groundwater flow and exchange across the land surface explain carbon export patterns in continuous permafrost watersheds. Geophys. Res. Lett. 45 (15), 7596–7605. https://doi.org/10.1029/2018GL078140.
- Nolan, M., 2003. Distribution of a Star3i DEM of the Kuparuk River Watershed. Joint Office for Scientific Support, Boulder, CO.
- O'Connor, M.T., Cardenas, M.B., Ferencz, S.B., Wu, Y., Neilson, B.T., Chen, J., Kling, G.W., 2020. Empirical models for predicting water and heat flow properties of permafrost soils. Geophys. Res. Lett. 47, e2020GL087646.
- O'Connor, M.T., Cardenas, M.B., Neilson, B.T., Nicholaides, K.D., Kling, G.W., 2019. Active layer groundwater flow: The interrelated effects of stratigraphy, thaw, and topography. Water Resources Research 55, 6555–6576.
- Painter, S.L., Coon, E.T., Atchley, A.L., Berndt, M., Garimella, R., Moulton, J.D., Svyatskiy, D., Wilson, C.J., 2016. Integrated surface/subsurface permafrost thermal hydrology: Model formulation and proof-of-concept simulations. Water Resourc. Res.

- 52 (8), 6062-6077.
- Paytan, A., Lecher, A.L., Dimova, N., Sparrow, K.J., Kodovska, F.G.-T., Murray, J., Tulaczyk, S., Kessler, J.D., 2015. Methane transport from the active layer to lakes in the Arctic using Toolik Lake, Alaska, as a case study. Proc. Natl. Acad. Sci. 112 (12), 3636–3640.
- Peltzer, G., Crampé, F., Hensley, S., Rosen, P., 2001. Geology 29 (11), 975–978. Ping, C.L., Bockheim, J.G., Kimble, J.M., Michaelson, G.J., Walker, D.A., 1998.
- High, C.L., Bockhelmi, J.C., Killole, J.M., Michaelson, G.J., Waiker, D.A., 1998. Characteristics of cryogenic soils along a latitudinal transect in Arctic Alaska. J. Geophys. Res. 103 (D22), 28917–28928.
- Ping, C.-L., Michaelson, G.J., Jorgenson, M.T., Kimble, J.M., Epstein, H., Romanovsky, V., Walker, D., 2008. High stocks of soil organic carbon in North American Arctic region. Nat. Geosci. 1, 615–619. https://doi.org/10.1038/ngeo284.
- Raymond, P., Hartmann, J., Lauerwald, R., Sobek, S., McDonald, C., Hoover, M., Butman, D., Striegl, R., Mayorga, E., Humborg, C., Kortelainen, P., Drr, H., Meybeck, M., Ciais, P., Guth, P., 2013. Global carbon dioxide emissions from inland waters. Nature 503, 355–359. https://doi.org/10.1038/nature12760.
- Rosen, P., Hensley, S., Joughin, I., Li, F.K., Madsen, S., Rodriguez, E., Goldstein, R.M., 2000. Synthetic aperture radar interferometry. Proc. IEEE 88 (3), 333–382. https://doi.org/10.1109/5.838084.
- Rouyet, L., Lauknes, T.R., Christiansen, H.H., Strand, S.M., Larsen, Y., 2019. Seasonal dynamics of a permafrost landscape, adventdalen, svalbard, investigated by Insar. Remote Sens. Environ. 231, 111236. https://doi.org/10.1016/j.rse.2019.111236.
- Sandwell, D.T., Price, E.J., 1998. Phase gradient approach to stacking interferograms. J. Geophys. Res. 103 (B12), 30183–30204.
- Sandwell, D., Myer, D., Mellors, R., Shimada, M., Brooks, B., Foster, J., 2008. Accuracy and resolution of alos interferometry: vector deformation maps of the father's day intrusion at Kilauea. Geosci. Remote Sensing 46, 3524–3534. https://doi.org/10. 1109/TGRS.2008.2000634.
- Schaefer, K., Liu, L., Parsekian, A., Jafarov, E., Chen, A., Zhang, T., Gusmeroli, A., Panda, S., Zebker, H.A., Schaefer, T., 2015. Remotely sensed active layer thickness (ReSALT) at Barrow, Alaska using Interferometric synthetic aperture radar. Remote Sens. 7 (4), 3735–3759. https://doi.org/10.3390/rs70403735.
- Schuur, E.A.G., Bockheim, J., Canadell, J.G., Euskirchen, E., Field, C.B., Goryachkin, S.V., Hagemann, S., Kuhry, P., Lafleur, P.M., Lee, H., Mazhitova, G., Nelson, F.E., Rinke, A., Romanovsky, V.E., Shiklomanov, N., Tarnocai, C., Venevsky, S., Vogel, J.G., Zimov, S.A., 2008. Vulnerability of permafrost carbon to climate change: implications for the global carbon cycle. BioScience 58 (8), 701–714. https://doi.org/10.1641/B580807.
- Short, N., Brisco, B., Couture, N., Pollard, W., Murnaghan, K., Budkewitsch, P., 2011. A comparison of TerraSAR-X, RADARSAT-2 and ALOS-PALSAR interferometry for monitoring permafrost environments, case study from Herschel Island, Canada. Remote Sens. Environ. 115 (12), 3491–3506. https://doi.org/10.1016/j.rse.2011.08. 012.
- Sjoberg, Y., Coon, E., Sannel, A.B.K., Pannetier, R., Harp, D., Frampton, A., Painter, S.L., Lyon, S.W., 2016. Thermal effects of groundwater flow through subarctic fens: A case study based on field observations and numerical modeling. Water Resourc. Res. 52 (3), 1591–1606.
- Strozzi, T., Antonova, S., Gnther, F., Matzler, E., Vieira, G., Wegmller, U., Westermann, S., Bartsch, A., 2018. Sentinel-1 sar interferometry for surface deformation monitoring in low-land permafrost areas. Remote Sensing 10 (9). https://doi.org/10.3390/rs10091360.
- Vidon, P., Allan, C., Burns, D., Duval, T.P., Gurwick, N., Inamdar, S., Lowrance, R., Okay, J., Scott, D., Sebestyen, S., 2010. Hot spots and hot moments in riparian zones: Potential for improved water quality management. JAWRA 46 (2), 278–298.
- Vonk, J., Gustafsson, O., 2013. Permafrost-carbon complexities. Nat. Geosci. 6, 675–676. https://doi.org/10.1038/ngeo1937.
- Walker, D., Binnian, E., Evans, B., Lederer, N.D., Nordstrand, E.A., Webber, P.J., 1989. Terrain, vegetation and landscape evolution of the R4D research site, Brooks Range Foothills, Alaska. Ecography 12, 238–261. https://doi.org/10.1111/j.1600-0587. 1989.tb00844.x.
- Walvoord, M.A., Striegl, R.G., 2007. Increased groundwater to stream discharge from permafrost thawing in the Yukon River basin: potential impacts on lateral export of carbon and nitrogen. Geophys. Res. Lett. 34 (12). https://doi.org/10.1029/ 2007GL030216.
- Wegmüller, U., Werner, C., Strozzi, T., Wiesmann, A., 2006. Ionospheric electron concentration effects on SAR and InSAR. In: Proc. IGARSS. vol. 6.
- Zebker, H.A., Villasenor, J., 1992. Decorrelation in interferometric radar echoes. IEEE Trans. Geosci. Remote Sens. 30 (5), 950–959. https://doi.org/10.1109/36.175330.
- Zebker, H.A., Werner, C.L., Rosen, P.A., Hensley, S., 1994. Accuracy of topographic maps derived from ERS-1 interferometric radar. IEEE Trans. Geosci. Remote Sens. 32 (4), 823–836. https://doi.org/10.1109/36.298010.
- Zebker, H.A., Rosen, P.A., Hensley, S., 1997. Atmospheric effects in Interferometric synthetic aperture radar surface deformation and topographic maps. J. Geophys. Res. 102 (B4), 7547–7563. https://doi.org/10.1029/96JB03804.
- Zebker, H.A., Hensley, S., Shanker, P., Wortham, C., 2010. Geodetically accurate InSAR data processor. Geosci. Remote Sensing 48 (12), 4309–4321. https://doi.org/10.1109/TGRS.2010.2051333.